6 Nonlinear Optical Microscopy

François Lagugné Labarthet and Yuen Ron Shen

6.1 Introduction

The constant evolution of optical microscopy over the past century has been driven by the desire to improve the spatial resolution and image contrast with the goal to achieve a better characterization of smaller specimens. Numerous techniques such as confocal, dark–field, phase–contrast, Brewster angle and polarization microscopies have emerged as improvement of conventional optical microscopy. Being a pure imaging tool, conventional optical microscopy suffers from its low physical and chemical specificity. This can be remedied by combining it with spectroscopic technique like fluorescence, infrared or Raman spectroscopy. Such microscopes have been successfully applied to the study of a wide range of materials with good spectral resolution. However their spatial resolution is restricted by the diffraction limit imposed by the wavelength of the probe light. In infrared microscopy, for instance, the lateral resolution is a few microns which is insufficient to resolve sub–micron structures. Conventional microscopy also does not provide microscopic information about the real surface structure of a specimen. Even in reflection geometry, they can only probe the structure of a surface layer averaged over a thickness of a reduced wavelength. Furthermore, they are insensitive to the polar organization of molecules in the layer although this could be important. In biophysics, for example, it is interesting to know the polar orientation of molecules adsorbed on a membrane and its influence on the membrane physiology.

In this context, nonlinear optical measurements used in conjunction with microscopy observation have created new opportunities [1]. Second–order nonlinear processes such as second harmonic (SH) or sum frequency generation (SFG) are highly surface–specific in media with inversion symmetry and uniquely suited for *in–situ* real–time investigation of surfaces and interfaces [2–4]. With their sub–monolayer surface sensitivity, SHG and SFG microscopies can be used to characterize inhomogeneities, impurities, formation of domains on surfaces or buried interfaces by mapping out the spatial variation of nonlinear susceptibilities at the interfaces. They are also sensitive to the orientation and distribution of molecules useful for evaluation of the structure and reactivity of a surface [5,6]. Third–order processes such as third harmonic generation (THG), coherent anti–Stokes Raman scattering (CARS) and two-photon excited fluorescence (TPEF) microscopies are of interest for the study of buried structures [7–9]. Because the output of second– and third– order processes scales, respectively, with the square and the cube of the excitation intensity, the focal excitation volume is greatly reduced, enhancing the depth resolution and reducing the out–of–focus background noise. This simple idea has stimulated the development of THG, CARS and TPEF microscopies in an effort to image buried structures in transparent materials or in biological tissues with a three dimensional sectioning capability. Using ultra–short pulses (10^{-12}–10^{-15} s) CARS has also been demonstrated to be a possible technique to probe the interior of living cells in real time [10].

Vibrational spectra are known as fingerprints of molecules. Nonlinear optical microspectrometry finds more interest in the mapping of localized domains via vibrational resonances. Microscopy with infrared (IR)–visible (Vis) sum frequency vibrational spectroscopy allows imaging of molecule–specific domains at a surface. Using a conventional far–field microscope, it can have a spatial resolution one order of magnitude better than Fourier–transform infrared microspectrometry. CARS microscopy also provides vibrational identification of chemical species and is an alternative way to conventional Raman confocal microscopy. Microspectrometry in the electronic transition region is also useful. Multiphoton fluorescence microscopy is becoming a standard technique for biological research [11]. In contrast to one–photon–excited fluorescence, multiphoton–excited fluorescence allows the use of input radiation in the transparent region of a sample and is capable of probing the interior structure of the sample with little laser–induced damages.

This brief introduction to nonlinear optical microscopy would be incomplete without mentioning the recent development in combining nonlinear optical measurements with near–field scanning optical microscopy (NSOM) techniques. In the past several years a growing number of studies of NSOM–SHG/SFG, NSOM–THG and NSOM–TPEF have been reported [12–15]. The spatial resolution of such optical microscopy is limited by the tip apex radius of the optic fiber; it varies from 20 to 200 nm depending on the techniques. In such an experiment, the sample–tip distance is maintained constant by using a feedback mechanism, which then also yields the surface topographical information. The latter can be correlated with the nonlinear NSOM result on specific molecular properties of the sample with a high spatial resolution. With short laser pulses, transient properties of nanostructures can also be probed.

In this chapter, we review a number of nonlinear optical techniques combined with microscope measurements that have been developed in recent years. We will describe separately, SHG, SFG, THG, CARS and multiphoton fluorescence microscopies. For each technique, we will first recall the underlying principle and describe the typical optical setup. We will then focus our interest on several chosen examples taken from the literature. Finally, the resolution limit as well as possible improvements of the various techniques will be discussed.

6.2 Second Harmonic Nonlinear Microscopy

6.2.1 Basic Principle of SHG

We describe here briefly the basic principle of SHG and the extension to the case of a strongly focused fundamental input beam. Details can be found elsewhere [16,17].

SHG originates from a nonlinear polarization $\boldsymbol{P}^{(2)}(2\omega)$ induced in a medium by an incoming field $\boldsymbol{E}(\omega)$:

$$\boldsymbol{P}^{(2)}(2\omega) = \varepsilon_0 \overleftrightarrow{\chi}^{(2)} : \boldsymbol{E}(\omega)\boldsymbol{E}(\omega), \tag{6.1}$$

where ε_0 is the vacuum permittivity and $\overleftrightarrow{\chi}^{(2)}$ denotes the nonlinear susceptibility of the medium. If the medium has inversion symmetry, then $\overleftrightarrow{\chi}^{(2)}$ for the bulk vanishes under the electric dipole approximation. At the surface or interface, however, the inversion symmetry is necessarily broken, and the corresponding $\overleftrightarrow{\chi}^{(2)}_{\mathrm{S}}$ is non–zero. This indicates that SHG can be highly surface–specific . As a result, SHG has been developed into a useful tool for many surface studies [18,19].

For SHG in reflected direction from a surface or interface, it has been shown that the output signal is given by

$$S(2\omega) = \frac{(2\omega)^2}{8\varepsilon_0 c^3 \cos^2\beta} \left|\chi^{(2)}_{\mathrm{eff}}\right|^2 [I(\omega)]^2 AT, \tag{6.2}$$

where β is the exit angle of the SH output, $I(\omega)$ is the beam intensity at ω, A is the beam area at the surface, T is the input laser pulse–width, and

$$\chi^{(2)}_{\mathrm{eff}} = \left(\overleftrightarrow{L}_{2\omega} \cdot \hat{\boldsymbol{e}}_{2\omega}\right) \cdot \overleftrightarrow{\chi}^{(2)}_{\mathrm{S}} : \left(\overleftrightarrow{L}_{\omega} \cdot \hat{\boldsymbol{e}}_{\omega}\right)\left(\overleftrightarrow{L}_{\omega} \cdot \hat{\boldsymbol{e}}_{\omega}\right), \tag{6.3}$$

with $\hat{\boldsymbol{e}}_{\omega}$ being the unit polarization vector and $\overleftrightarrow{L}_{\omega}$ the Fresnel factor at frequency ω. The surface nonlinear susceptibility $\overleftrightarrow{\chi}^{(2)}_{\mathrm{S}}$ is related to the molecular hyperpolarizability $\overleftrightarrow{\alpha}^{(2)}$ by a coordinate transformation

$$\left(\chi^{(2)}_{S}\right)_{ijk} = N_{\mathrm{S}} \sum_{i'j'k'} \left[\alpha^{(2)}_{i'j'k'} \left\langle (\hat{\boldsymbol{i}} \cdot \hat{\boldsymbol{i}}')(\hat{\boldsymbol{j}} \cdot \hat{\boldsymbol{j}}')(\hat{\boldsymbol{k}} \cdot \hat{\boldsymbol{k}}') \right\rangle\right], \tag{6.4}$$

where i, j, k and i', j', k' stand for the laboratory and molecular coordinate axes, the angular brackets refer to an average over the molecular orientational distribution, and N_{S} is the surface density of molecules. At a surface of high symmetry, only a few $(\chi^{(2)}_{\mathrm{S}})_{ijk}$ elements are independent and nonvanishing. They can be determined from SHG measurements with different input/output polarizations. From $(\chi^{(2)}_{\mathrm{S}})_{ijk}$ together with knowledge of $\alpha^{(2)}_{i'j'k'}$, an approximate orientational distribution of the molecules could be deduced.

From (6.4), it is seen that spatial variation of molecular species, molecular density, and molecular orientation and arrangement can lead to spatial variation of $\overleftrightarrow{\chi}^{(2)}_{\mathrm{S}}$. Such variation on the micrometer or nanometer scale could be probed by SHG microscopy.

The above theoretical description of SHG assumes the usual plane–wave approximation. However, SHG microscopy often requires a strongly focused input laser beam. Obviously, (6.2) for SHG output has to be modified by a geometric factor to take into account the focusing geometry. Fortunately, this geometric factor should remain unchanged as the focal spot scans over a flat surface, and therefore the spatial variation of the SHG output should still reflect the spatial variation of $|\chi^{(2)}_{\mathrm{eff}}|^2$ over the surface, yielding a surface microscope image.

Geometries for Second Harmonic Far–Field Microscopy The first experiments of second harmonic microscopy were performed in the middle of the seventies by Hellwarth and Christensen [20]. In these experiments, grain structures and defects localized at the surface of thin films of nonlinear materials (ZnSe, GaAs, CdTe) were imaged by the second harmonic signal ($\lambda = 532$ nm) generated in the transmitted direction using a nanosecond pulsed Nd:YAG laser. Boyd and coworkers [21] first demonstrated the possibility of SH microscopy imaging of a surface monolayer. Even with a crude focusing and scanning setup, they were able to observe SHG in reflection, with a spatial resolution of several microns, from a hole burned in a Rhodamine 6G monolayer deposited on a silica substrate. Later, Schultz *et al.* [22,23] used SH microscopy to study surface diffusion of Sb adsorbates on Ge. They adopted the parallel imaging scheme with a photodiode array. The spatial resolution limited by the pixel size of the 2–D detector was estimated to be ~ 5 μm. With the use of a 5 ns and 10 Hz pulsed Nd:YAG laser beam as the pump source, an acquisition time of 5–10 minutes was required.

In recent years, tremendous progress on laser technology, imaging systems, photodetectors and scanning devices has been made. This facilitates the development of SH microscopy. On the other hand, growing interest in surfaces, surface monolayers and thin films has also fostered the interest in SH microscopy [24]. The technique has been applied to the study of a wide range of surfaces and interfaces including Langmuir monolayers at the air–water interface [25], multilayers assemblies [26], self assembled monolayers [27], metallic [28] and semiconductors surfaces [29–31], nonlinear optical materials [32–34], and biomembranes [35–38].

Using a nsec Q–switched Nd:YAG laser and a CCD detector array, Flörsheimer and coworkers has developed SH microscopy in various geometries (Fig. 6.1a–d) and applied it to Langmuir monolayers [5,39–42]. Variation of the polarizations of the input and output beams allows the determination of polar orientation of molecules in microdomains. As examples, the SH microscopy images of a Langmuir monolayer of a 2–docosylamino–5–nitropyridine (DCANP) on water are displayed in Fig. 6.1e and f. They were obtained with the beam geometry described in Fig. 6.1d and the input/output polarization combinations depicted in Fig. 6.1g and h, respectively. A domain size of a few μm can be easily resolved.

In simple cases like 2–docosylamino–5–nitropyridine (DCANP), the nonlinear polarizability of the molecules can be approximated by a single tensor element $\alpha^{(2)}_{zzz}$ along the molecular axis $\hat{z}$. If the molecules are well aligned in a monolayer domain, then the nonlinear susceptibility of the domain is also dominated by a single tensor element $\chi^{(2)}_{Z'Z'Z'}$ along the alignment direction $\hat{\boldsymbol{Z}}'$. In this case, the *s*–in/*s*–out polarization combination of SHG probes an effective nonlinear susceptibility

$$\left|\chi^{(2)}_{\mathrm{eff}}\right|_{ss} = \left|F_{ZZ}\chi^{(2)}_{ZZZ}\sin^3\phi\right| = \left|F_{ZZ}\chi^{(2)}_{Z'Z'Z'}\cos^3\theta\sin^3\phi\right| , \tag{6.5}$$

where θ is the tilt angle of $\hat{\boldsymbol{Z}}'$ from the surface plane, ϕ is the angle between the incidence plane and $\hat{\boldsymbol{Z}}$, which is the projection of $\hat{\boldsymbol{Z}}'$ on the surface, and F_{ZZ} is the product of the three relevant Fresnel factors (see (6.3)). The beam geometry of Fig. 6.1g corresponds to such a case.

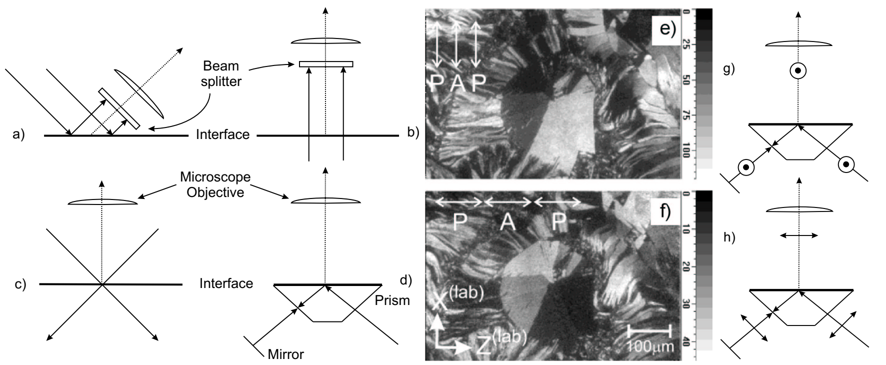

Fig. 6.1. (**a**,**b**,**c**,**d**) Schemes of the second harmonic microscopes using various geometries. (**e**,**f**) SH micrographs of a DCANP Langmuir film at the surface of water. Image (**e**) is obtained using the *ss* polarization configuration (**g**) while image (**f**) is obtained using the *pp* polarization configuration (**h**) [5]

For the beam geometry of Fig. 6.1h, the effective nonlinear susceptibility deduced is

$$\begin{aligned}\left|\chi_{\text{eff}}^{(2)}\right|_{pp} &= \left|F_{ZZ}\cos^2\beta_1\cos^3\phi\chi_{ZZZ}^{(2)} + F_{ZY}\sin^2\beta_1\cos\phi\chi_{ZYY}^{(2)}\right| \\ &= \left|\left(F_{ZZ}\cos^2\beta_1\cos^3\theta\cos^3\phi + F_{ZY}\sin^2\beta_1\cos\theta\sin^2\theta\cos\phi\right)\chi_{Z'Z'Z'}^{(2)}\right|,\end{aligned} \tag{6.6}$$

where β_1 is the incidence angle of the fundamental input, F_{ZZ} and F_{ZY} are the respective products of Fresnel factors, and $z-y$ defines the incidence plane. It is seen from (6.5) that the Z direction can be determined from the variation of SHG with ϕ with the s–in/s–out polarization. Then from (6.5) and (6.6), $\chi_{Z'Z'Z'}^{(2)}$ and θ can be deduced if β_1 is known and $(\chi_{\text{eff}}^{(2)})_{ss}$ and $(\chi_{\text{eff}}^{(2)})_{pp}$ are measured. Thus the various domains in Fig. 6.1e and f clearly correspond to domains of different molecular alignments.

SH microscopy has also been used to probe three dimensional structures of biological tissues and defects in materials. In this case, SHG originates from the focal region in the bulk. Using a reflection geometry and femtosecond pulses from a mode–locked dye laser, Guo *et al.* [43] have obtained SH images of skin tissues. In their setup, a 27× microscope objective was used for both excitation and collection of SHG, and the sample was mounted on a XYZ stage for lateral and axial movement, allowing 3–D imaging of a fascia membrane and muscle attached to the biological tissue. Interpretation of the images in term of molecular organization could be improved by analyzing the polarization dependence of the collected signal. In the case of the muscles tissues, *in–vivo* investigations could also be of interest to monitor the physiological change of the fibrils membranes under stress.

Gauderon *et al.* [44] have used femtosecond pulses from a Ti:sapphire laser to obtain by reflection 3–D SH microscopy images of lithium triborate (LBO) crystal fragments embedded in agar. The experimental arrangement in shown in Fig. 6.2a. The sample on the scanning stage was scanned by the focused laser beam both laterally and axially. A typical image is presented in Fig. 6.2b describing a scanned volume of 70 µm × 70 µm × 30 µm. Terraces, isolated microcrystallites and columnar arrangements of the crystal fragments are clearly observed. The spatial resolution of the image depends on the dimensions of the focal point. Since SHG is proportional to the square of the local fundamental input intensity, the effective point–spread function of the SH output is smaller than that of the input by a $\sqrt{2}$ factor allowing a resolution of $0.61\lambda/(\sqrt{2}\mathrm{NA})$, where λ is the input wavelength and NA denotes the numerical aperture of the focusing lens. With λ=790 nm and NA = 0.8 this lead to a spatial resolution of 0.4 µm, that is comparable to the maximum resolution obtained in confocal linear optical microscopy. It could be further improved using a confocal pinhole in the detection optics.

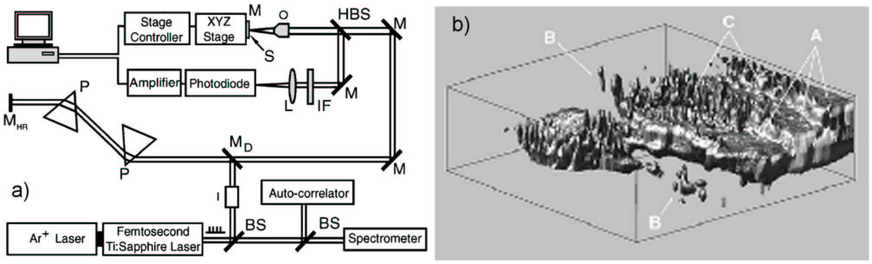

Fig. 6.2. (**a**) Optical setup used for SH tomographic imaging in the reflectance mode. BS: beam splitter, HBS: harmonic dichroic filter, L: lens, M: mirrors, O: objective, P: prisms, S: sample. (**b**) 3–D second harmonic generation(70 µm × 70 µm × 30 µm) of lithium triborate crystal fragments. Terraces (A), isolated crystallites (B), columnar stacking (C), can be identified [44]

6.2.2 Coherence Effects in SH Microscopy

In SH microscopy, interferences from various features on the surface and/or background can lead to severe distortion of the SH image although, in most studies, such effects have not been taken into account. Parallel (non–scanning) SHG imaging using a 2–D detector array, for example, could suffer from interferences between contributions originating from different sites of the sampled area. On the other hand, despite longer acquisition time, the local nature of a scanning focused fundamental beam reduces interference effects and the morphology interpretation of images is generally more straightforward [45].

However, even if the fundamental beam is tightly focused, the coherent nature of SHG implies that the sample signal can still be distorted by background contribution from sources other than the sample [46]. To cancel a uniform background contribution, one can insert a NLO crystal in the optical pathway [45,47]. By adjusting the crystal orientation properly, it is possible to generate a SH field from the crystal with proper phase and amplitude to cancel the background SH field. Figure

6.3 shows an example. The original SH microscopy image of a damaged area of Si–SiO_2 interface has two minima and a central peak. After the background suppression, only the central peak with a slightly larger width is observed. The same background correction scheme may not work with the parallel imaging method if the background contribution is non–uniform over the probed area.

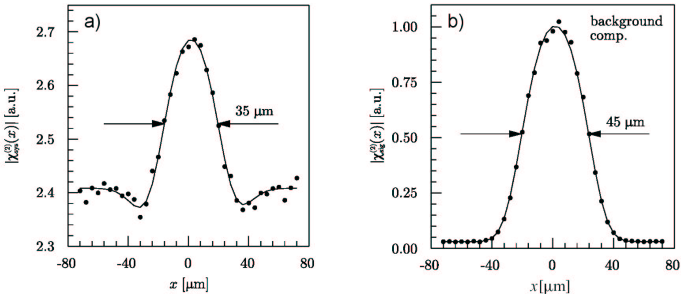

Fig. 6.3. (**a**) SH signal profile of a damaged area before correction of the background contribution. The step size is 4 µm and the dwell time at each sample spot was 5 s. (**b**) Damaged area after background compensation [47]

One can utilize the interference effect to obtain phase–contrast microscope images. In a recent experiment, Flörsheimer *et al.* [48] coherently mix the SH wave generated from a sample (interface) with the reference SH wave from a crystalline quartz plate. The resultant SH wave has a spatial intensity variation depending on $\cos[(\phi_S(\boldsymbol{r}) - \phi_R]$ where ϕ_S and ϕ_R are the phases of the SH waves from the sample and the reference, respectively. The microscope image then reflects the spatial variation of $\phi_S(\boldsymbol{r})$, which can provide additional information concerning the sample.

6.2.3 Scanning Near–Field Nonlinear Second Harmonic Generation

Far–field SH microscopy still has a spatial resolution limited to μm^2. Incorporation of near–field optics in SH microscopy overcomes the diffraction limit and allows studies of nanosructures. Near–field SHG measurements on rough metallic surfaces [49], ferroelectric domains [50], piezoceramics [51], and LB films [12] have been reported.

The first near–field SHG images were obtained by Bozhevolnyi *et al.* [12,52]. Their experimental setup (Fig. 6.4a) is a NSOM with a shear–force–based feedback system. The femtosecond fundamental input pulses from a mode–locked Ti:sapphire laser irradiate the sample through a single–mode fiber with an uncoated sharp tip, and both the fundamental and the SH output in the transmitted direction are collected by photodetectors. The fiber tip has its axial position controlled by the tuning fork sensor technique [53]. The scheme then allows the mapping of surface topography with a few nm resolution like that in atomic force microscopy when the sample surface is scanned. The topography can be correlated with the observed spatial variations of the fundamental and SH outputs from the sample. As an example, Fig. 6.4b presents the three images of a $LiNbO_3$ crystal with three small scatterers on it. All the three images display the presence of the unidentified particles at the surface. In the fundamental and SH images, the particles appear as dark spots. The decrease of signals over the particles is presumably due to scattering loss as the tip moves over the particles. The observed lateral resolution of SH–NSOM was around 100–150 nm in the experiments that map the domain edges of a Langmuir–Blodgett film [12,52] and a quasi–phase matching crystal [54]. Similar resolution was obtained by Smolyaninov *et al.* [51].

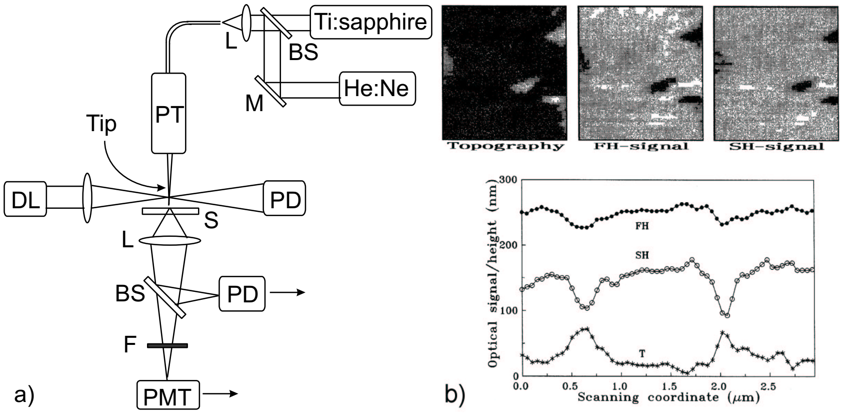

Fig. 6.4. (**a**) Experimental setup for local probing of second–order susceptibilities with a near–field optical microscope. BS: beam splitters, M: mirror, L: micro–objectives, S: sample, PT: piezo translators, DL: diode laser, PD: photodiodes, F: filter and PMT: photomultiplier tube. The detected second harmonic power versus the pump power squared is shown in the inset. (**b**) Topography, fundamental and SH near–field images ($2.5 \times 3\ \mu m^2$) of a $LiNbO_3$ crystal with corresponding cross–sections of these images. The images were recorded simultaneously with a total acquisition time of 9 minutes [52]

There are many variations of beam geometry in SHG–NSOM. With the fundamental input incident on a sample through a fiber tip, the SH output can be detected either in the transmitted and reflected direction. It is also possible to use a fiber tip to collect near–field SHG from a sample which is broadly illuminated by the fundamental input. One can also have SHG in an evanescent mode and use a metal tip close to the sample surface to induce a SH leak from the surface.

As is true for all NSOM, the theoretical description of SHG–NSOM is difficult. The attempts to model SHG–NSOM have been reported recently [55–57]. The SH signal depends in a complicated way on the polarization of the fundamental field, and multiple scattering of both the fundamental and the SH waves in the medium must be taken into account. Thus, unlike in far–field SHG, little information can be deduced from the polarization dependence of SHG–NSOM. Near–field SHG from mesoscopic structures using either the tip illumination mode [58] or the tip collection mode [59] has been described by a self–consistent integral equation formalism. The calculation shows a strong localization of the SH field around the mesostructures in both lateral and axial dimensions. This strong 3–D localization of SHG is of particular interest to imaging of nanostructures with a NSOM.

6.3 Sum Frequency Generation Microscopy

6.3.1 Basic Principle of Sum Frequency Generation

As a second–order nonlinear optical process, sum frequency generation (SFG) is also highly surface–specific in media with inversion symmetry, and can be used as a surface probe. The IR–Vis SFG has already been developed into a powerful surface vibrational spectroscopic technique [60,61]. In IR–Vis SFG, a visible laser pulse (ω_{Vis}) overlaps with a infrared pulse (ω_{IR}) at a surface and induces a nonlinear polarization $\boldsymbol{P}^{(2)}$ at the sum frequency $\omega_{\mathrm{SF}} = \omega_{\mathrm{Vis}} + \omega_{\mathrm{IR}}$:

$$\boldsymbol{P}^{(2)}(\omega_{\mathrm{SF}} = \omega_{\mathrm{Vis}} + \omega_{\mathrm{IR}}) = \varepsilon_0 \overleftrightarrow{\chi}^{(2)} : \boldsymbol{E}(\omega_{\mathrm{Vis}})\boldsymbol{E}(\omega_{\mathrm{IR}}), \tag{6.7}$$

which radiates and generates the SF output. As in SHG (6.2), the SF output in the reflected direction is given by:

$$S(\omega_{\mathrm{SF}}) \propto \left|\chi^{(2)}_{\mathrm{eff}}(\phi)\right|^2 I(\omega_{\mathrm{Vis}})I(\omega_{\mathrm{IR}})AT, \tag{6.8}$$

with

$$\chi^{(2)}_{\mathrm{eff}}(\phi) = \left(\overleftrightarrow{L}_{\omega_{\mathrm{SF}}} \cdot \hat{\boldsymbol{e}}_{\omega_{\mathrm{SF}}}\right) \cdot \overleftrightarrow{\chi}^{(2)}_{\mathrm{S}} : \left(\overleftrightarrow{L}_{\omega_{\mathrm{Vis}}} \cdot \hat{\boldsymbol{e}}_{\omega_{\mathrm{Vis}}}\right)\left(\overleftrightarrow{L}_{\omega_{\mathrm{IR}}} \cdot \hat{\boldsymbol{e}}_{\omega_{\mathrm{IR}}}\right) \tag{6.9}$$

and $\overleftrightarrow{\chi}^{(2)}_{\mathrm{S}}$ is related to the molecular hyperpolarizability $\overleftrightarrow{\alpha}^{(2)}$ by (6.4). If ω_{IR} is tuned over vibrational resonances, $\overleftrightarrow{\alpha}^{(2)}$ must exhibit corresponding resonance enhancement and can be expressed in the form

$$\overleftrightarrow{\alpha}^{(2)} = \overleftrightarrow{\alpha}^{(2)}_{\mathrm{NR}} + \sum_q \frac{\overleftrightarrow{a}_q}{(\omega_{\mathrm{IR}} - \omega_q) + i\Gamma_q}, \tag{6.10}$$

where $\overleftrightarrow{\alpha}^{(2)}_{\mathrm{NR}}$ is the non–resonant contribution and $\overleftrightarrow{a}_q$, ω_q and Γ_q denote the strength, resonant frequency and damping constant of the qth vibrational mode, respectively. Correspondingly, we have

$$\overleftrightarrow{\chi}^{(2)}_{\mathrm{S}} = \overleftrightarrow{\chi}^{(2)}_{\mathrm{NR}} + \sum_q \frac{\overleftrightarrow{A}_q}{(\omega_{\mathrm{IR}} - \omega_q) + i\Gamma_q}. \tag{6.11}$$

If the infrared input is tunable and scans over vibrational resonances, the resonant enhancement of the SF output naturally yields a surface vibrational spectrum. Such spectra with different input/output polarization combinations can yield information about surface composition and structure in a local surface region. This technique has found many applications in many areas of surface science. However, only a few studies combining SFG vibrational spectroscopy and optical microscope techniques have been reported.

6.3.2 Far–Field SFG Microscopy

Combination of SF vibrational spectroscopy with optical microscopy allows detection or mapping of selective molecular species at a surface or interface. It also has the advantage of an improved spatial resolution in comparison to conventional FTIR microscopy because the resolution is now limited by the SF wavelength instead of the IR wavelength. This is similar to Raman microscopy, but the latter is not surface specific.

Flörsheimer has extended his development of SH microscopy to SF microscopy [5,42]. The experimental arrangement with the input beams in total reflection geometry is depicted in Fig. 6.5a. A Langmuir–Blodgett monolayer film to be imaged is adsorbed on the base surface of a prism. Two input beams enter by the two hypotenuse faces of the prism and the SF output exits from the film surface at an oblique angle.

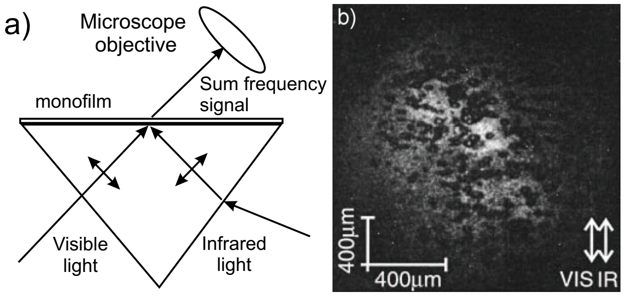

Fig. 6.5. (**a**) The thin film is deposited on the prism and is illuminated with two *p*–polarized pulsed beams, ω_{Vis} and ω_{IR}, impinging on the film in the total reflection geometry. The visible frequency, ω_{Vis}, is fixed at 18800 cm^{-1} and the infrared frequency, ω_{IR}, is tunable. No output analyzer is used and the SF signal is found to be mainly *p* polarized. (**b**) Sum frequency image of a LB monolayer of arachidic acid. The infrared frequency (2962 cm^{-1}) is tuned to the anti–symmetric stretching mode of methyl groups. Note that the scale bars are not of equal size due to the oblique incidence of the collecting objective. Figure 6.5b is reprinted with permission from [42]. Copyright (1999) American Chemical Society

Figure 6.5b shows an SFG image of a monolayer of arachidic acid molecules obtained with parallel imaging with the IR frequency set at 2962 cm^{-1} in resonance with the CH_3 stretching mode. The image exhibits dark holes and clear non–uniformity in the illumination region. Similar experiment with the IR frequency at 2850 cm^{-1} in resonance with the methylene stretch yielded little SF signal. These results indicate that the alkyl chains of the monolayer are in nearly all–trans configuration. The bright areas in the image in Fig. 6.5b represent regions with a densely packed molecules in trans conformation. The dark holes likely originate from a lack of molecules in the areas. They were not observed in freshly prepared LB films, but appeared and grew with time due to a dewetting or desorption.

In the experimental geometry of Fig. 6.5a, emission of SF output at an oblique angle could lead to image distortion in the parallel imaging process and deterioration of spatial resolution. The problem could be solved by having the SF output emitted normal to the surface. Unfortunately this may not be possible with the total–reflection geometry described in Fig. 6.5a. Matching of wave–vector components along the surface would require that the visible input beam be transmissive at the surface.

6.3.3 Near–Field SFG Imaging

Spatial resolution of SF microscopy can be improved to much below micron scale by near–field detection of the SF output, as demonstrated independently by Shen *et al.* [13], Schaller and Saykally [62] and Humbert *et al.* [63]. However, so far, only studies of SFG–allowed media have been reported.

The experimental setup of Shen *et al.* is described in Fig. 6.6a. It allows near–field imaging of SHG and SFG as well as topography of a sample with a lateral resolution of about 120 nm. The wavelengths of the two input beams from a nsec laser are fixed at 1.047 μm and 0.524 μm in the experiment. SHG and SFG from the sample deposited on the base surface of the prism are generated in the total reflection mode. The spatial variations of the evanescent waves above the sample surface are probed via optical tunneling by an Al–coated fiber with a 120 nm aperture attached to an XYZ piezoelectric scanner. With a shear force feedback to keep the probe–sample distance constant, the fiber tip also yields the surface topography as the probe scans the sample surface. Figure 6.6b shows the surface topography as well as the SH and SF microscopy images of three isolated NNP (N–(4–nitrophenyl)–(L)–prolinol) nanocrystals of ~360 nm in size that were deposited on the prism surface. The three images appear to be well correlated.

Schaller and Saykally [62] have performed near–field SFG microscopy with a tunable IR input. They adopted a commercial NSOM head for collection of the SF output (Fig. 6.7a). A femtosecond Ti:sapphire laser was used to provide the visible

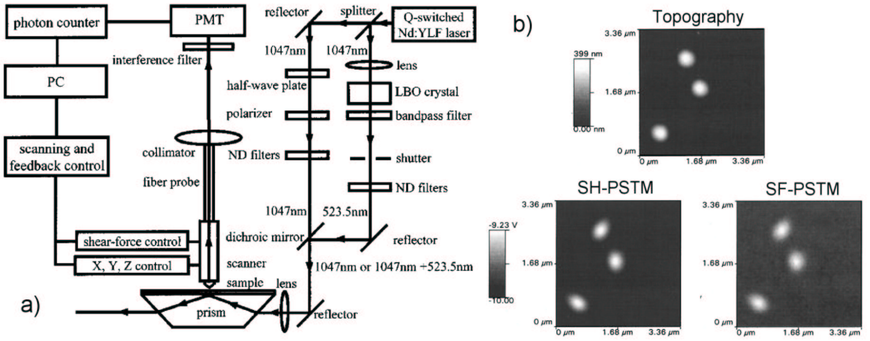
photon counter
PMT
interference filter
PC
scanning and feedback control
collimator
fiber probe
shear-force control
X, Y, Z control
scanner
sample
lens
prism
reflector
splitter
Q-switched Nd:YLF laser
1047nm
1047nm
lens
half-wave plate
LBO crystal
polarizer
bandpass filter
ND filters
shutter
ND filters
1047nm
523.5nm
dichroic mirror
reflector
1047nm or 1047nm +523.5nm
reflector
a)
b)
Topography
399 nm
0.00 nm
3.36 μm
1.68 μm
0 μm
0 μm
1.68 μm
3.36 μm
SH-PSTM
-9.23 V
-10.00
3.36 μm
1.68 μm
0 μm
0 μm
1.68 μm
3.36 μm
SF-PSTM
3.36 μm
1.68 μm
0 μm
0 μm
1.68 μm
3.36 μm

Fig. 6.6. (**a**) Optical set up used for both SHG and SFG photon scanning tunneling microscopy. (**b**) Topography, SH and SF images of NNP nanocrystals [13] input and to pump an optical parametric amplifier/difference frequency generator system to generate the tunable IR input. The microscopy was applied to a thin film of ZnSe with the IR wavelength varied from 3.1 to 4.4 μm. Figure 6.7b shows the surface topography and SF images at two IR wavelengths for a 10 μm^2 area of the sample. The SF images reveals strain patterns that are not observable in the surface topography. The lateral spatial resolution is estimated to be about 1/20 of the IR wavelength.

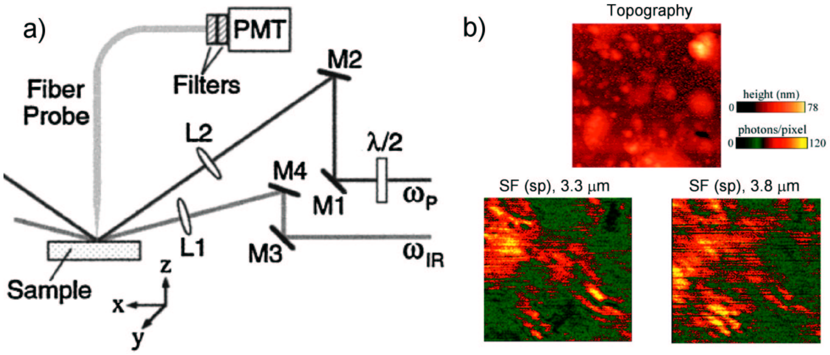

Fig. 6.7. (**a**) Setup for SFG–NSOM. The uncoated NSOM fiber probe tip (apex ~50 nm) operates in the collection mode. Infrared light is tunable from 2.8 to 10 μm. The two input beams overlap over a surface of 100 μm^2. (**b**) Topographic and SFG images (10 μm^2) of ZnSe thin film deposited on a substrate by chemical vapor deposition. Topographic and SH images are simultaneously acquired in 30 min. The spatial resolution is estimated to be 190 nm. Reprinted with permission from [62]. Copyright (2001) American Chemical Society

6.4 Third Harmonic Generation Microscopy

While second–order nonlinear optical processes require a medium without inversion symmetry, third–order processes such as third–harmonic generation are allowed in any medium. The nonlinear polarization induced in a medium responsible for THG is

$$\boldsymbol{P}^{(3)}(3\omega) = \varepsilon_0 \overleftrightarrow{\chi}^{(3)} : \boldsymbol{E}(\omega)\boldsymbol{E}(\omega)\boldsymbol{E}(\omega), \tag{6.12}$$

where $\overleftrightarrow{\chi}^{(3)}$ is the third–order nonlinear susceptibility for the process. In the plane wave approximation, the TH output is given by

$$S(3\omega) \propto \left|\chi^{(3)}_{\text{eff}}(\phi)\right|^2 I(\omega)I(\omega)I(\omega), \tag{6.13}$$

with,

$$\chi^{(3)}_{\text{eff}}(\phi) = \left(\overleftrightarrow{L}_{3\omega} \cdot \hat{\boldsymbol{e}}_{3\omega}\right) \cdot \overleftrightarrow{\chi}^{(3)} : \left(\overleftrightarrow{L}_{\omega} \cdot \hat{\boldsymbol{e}}_{\omega}\right)\left(\overleftrightarrow{L}_{\omega} \cdot \hat{\boldsymbol{e}}_{\omega}\right)\left(\overleftrightarrow{L}_{\omega} \cdot \hat{\boldsymbol{e}}_{\omega}\right). \tag{6.14}$$

If the fundamental input beam is strongly focused in the bulk of the medium, then the TH output becomes [64,17]

$$S_{3\omega} \propto P_{\omega}^{3} \left| \int_{0}^{l} \frac{\chi^{(3)}(z')\exp(i\mathit{\Delta}\boldsymbol{k}z')\mathrm{d}z'}{(1+2\mathrm{i}z'/b)^{2}} \right|^{2}, \tag{6.15}$$

where the integration extends over the length of the medium, P_ω is the fundamental beam power, $\boldsymbol{k}_\omega$ and $\boldsymbol{k}_{3\omega}$ are the wave vectors at ω and 3ω, respectively, $b = \boldsymbol{k}_\omega.w_0^2$ is the confocal parameter of the fundamental beam with a waist radius of w_0 and $\mathit{\Delta}\boldsymbol{k} = 3\boldsymbol{k}_\omega - \boldsymbol{k}_{3\omega}$ is the phase mismatch. The integration in (6.15) nearly vanishes if $\mathit{\Delta}\boldsymbol{k} \leq 0$ and $l \gg 1/\mathit{\Delta}\boldsymbol{k}$ but is finite for $\mathit{\Delta}\boldsymbol{k} > 0$ [17]. However, in a medium with normal dispersion, we expect $\mathit{\Delta}\boldsymbol{k} < 0$ and hence a vanishing THG. Since third order nonlinearity away from resonance is generally very weak and tight focusing for THG is often required, this is obviously a shortcoming for using THG as a probe. Nevertheless, Tsang has pointed out that with focusing at an interface, the symmetry of the focusing geometry is broken and (6.15) needs to be modified [65]. Then even with $\mathit{\Delta}\boldsymbol{k} < 0$, THG in the forward direction can be appreciable.

In combination with a transmission optical microscope, THG can be used to image a transparent sample with a 3–D microscopy capability. Indeed, liquid crystal phase transitions [66], semiconductor microstructures [67], optical fiber structures [68,69] and biological samples [7,70] have been investigated with this technique. Recently, Schaller *et al.* have imaged red blood cells using THG–NSOM [14].

To illustrate the 3–D imaging capability of THG microscopy, we present in Fig. 6.8 the experimental setup and result of Squier *et al.* [71]. A regeneratively amplified femtosecond Ti:sapphire laser is used to pump an optical parametric amplifier, whose output is focused on the sample for TH imaging. The sample is mounted on an *XYZ* scanning stage. Figure 9.6 in Chap. 6.7 shows an example of such an image. The 3–D array of letters inscribed in a glass can be recognized with micron resolution.

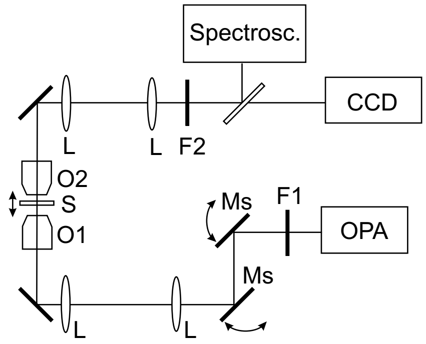

Fig. 6.8. Optical setup used by Squier *et al.* for both writing and reading microdamage patterns in optical glass: OPA: optical parametric amplifier, F1: long pass filter, Ms: scanning mirrors, O1 and O2: objective lenses, F2: blocking filter, M1: insertable mirror [71]

6.5 Coherent Anti–Stokes Raman Scattering Microscopy

Similar to THG, coherent anti–Stokes Raman scattering (CARS) is a third order four–wave mixing process but is resonantly enhanced at vibrational resonances, and is a powerful vibrational spectroscopic tool [72]. The process involves two input waves at frequencies ω_P and ω_S with $\omega_\mathrm{P} - \omega_\mathrm{S}$ tuned to a vibrational resonance of the medium. The two inputs overlap in the medium and induce a third–order nonlinear polarization in the medium at the anti–Stokes frequency $\omega_\mathrm{AS} = 2\omega_\mathrm{P} - \omega_\mathrm{S}$:

$$\boldsymbol{P}^{(3)}_{\omega_\mathrm{AS}} = \epsilon_0 \overleftrightarrow{\chi}^{(3)} : \boldsymbol{E}(\omega_\mathrm{P})\boldsymbol{E}(\omega_\mathrm{P})\boldsymbol{E}^*(\omega_\mathrm{S}), \tag{6.16}$$

which is the radiation source for CARS. Similar to SFG (6.11), the nonlinear susceptibility can be written as the sum of a non–resonant and a resonant term:

$$\overleftrightarrow{\chi}^{(3)} = \overleftrightarrow{\chi}^{(3)}_\mathrm{NR} + \sum_q \frac{\overleftrightarrow{A}_q}{(\omega_\mathrm{P} - \omega_\mathrm{S}) - \omega_q + i\Gamma_q}. \tag{6.17}$$

Under the plane–wave approximation, the CARS output intensity from a uniform sample of thickness d is given by

$$S(\omega_\mathrm{AS}) \propto \left|\chi^{(3)}_\mathrm{eff}\right|^2 I_\mathrm{P}^2 I_\mathrm{S} \sin^2\left(|\Delta\boldsymbol{k}|\, d/2\right) / |\Delta\boldsymbol{k}|^2 , \tag{6.18}$$

where $\Delta\boldsymbol{k} = 2\boldsymbol{k}_\mathrm{P} - \boldsymbol{k}_\mathrm{S} - \boldsymbol{k}_\mathrm{AS}$ and

$$\chi^{(3)}_\mathrm{eff} = \left(\overleftrightarrow{L}_{\omega_\mathrm{AS}} \cdot \hat{\boldsymbol{e}}_{\omega_\mathrm{AS}}\right) \cdot \overleftrightarrow{\chi}^{(3)} : \left(\overleftrightarrow{L}_{\omega_1} \cdot \hat{\boldsymbol{e}}_{\omega_1}\right)\left(\overleftrightarrow{L}_{\omega_1} \cdot \hat{\boldsymbol{e}}_{\omega_1}\right)\left(\overleftrightarrow{L}_{\omega_2} \cdot \hat{\boldsymbol{e}}_{\omega_2}\right). \tag{6.19}$$

In the case of a strongly focused geometry or a heterogeneous medium, (6.18) needs to be modified, but the characteristic dependence of the CARS output on the phase matching $\Delta\boldsymbol{k}$ is still approximately true. For CARS generated in the forward direction (F–CARS), $|\Delta\boldsymbol{k}|$ is generally much smaller than $1/\lambda_\mathrm{AS}$. For CARS generated in the backward direction (E–CARS, where E stands for epi–detection), $|\Delta\boldsymbol{k}|$ is larger than $2\pi/\lambda_\mathrm{AS}$. From a thin sample, F–CARS and E–CARS, both having $|\Delta\boldsymbol{k}|d \ll \pi$, are expected to have nearly the same signal intensity. From a thick sample with $|\Delta\boldsymbol{k}|d < \pi$ for F–CARS but $|\Delta\boldsymbol{k}|d \gg \pi$ for E–CARS, F–CARS should have a much stronger output than E–CARS.

Xie and coworkers [10,73] have studied theoretically the ratio of E–CARS and F–CARS outputs in strongly focusing geometry by varying the sample thickness d. They show that the E–CARS output reaches the relative maximum at d=$0.65\lambda_\mathrm{P}$. Incorporation of CARS into optical microscopy provides microspectrometric imaging of materials. Duncan and coworkers first used CARS microscopy with psec laser pulses to image biological cells soaked in deuterated water [74–76] . Asides from being able to selectively map out distributions of molecular species via their vibrational resonances, it also has a number of other advantages compared to, in particular, Raman spectroscopy. (1) Since the CARS intensity (6.18) is proportional to $I_\mathrm{P}^2 I_\mathrm{S}$, both the lateral and the axial resolution are $\sim \sqrt{3}$ times better than that of linear optical microscopy. For $\omega_P - \omega_S$=3053 cm^{-1} (CH ring stretching mode), a lateral resolution around 300 nm and an axial resolution around 1.6 µm (even without a confocal pinhole) have been obtained [77]. (2) A moderate laser intensity and power can be used to avoid damaging of biological samples like living cells. (3) The anti–Stokes emission in CARS is spectrally separable from fluorescence as its wavelength is shorter than λ_P. (4) Transparency of the medium to the input waves allows 3–D microscopy and imaging of buried samples.

Recently, Zumbusch *et al.* [77] and Volkmer *et al.* [73] have developed F–CARS and E–CARS microscopy in the 2600–3300 cm^{-1} region using femtosecond pulses generated by a Ti:sapphire laser and an associated optical parametric oscillator/amplifier (Fig. 6.9a). The input beams are focused through a 60× oil–immersion objective with NA=1.4. A similar objective was used to collect the signal in both forward and backward directions. The broad spectral width of femtosecond pulses limits the spectral resolution to ~ 60 cm^{-1}, as seen in Fig. 6.9b. For better spectral resolution longer input pulses with a narrower spectral width are required.

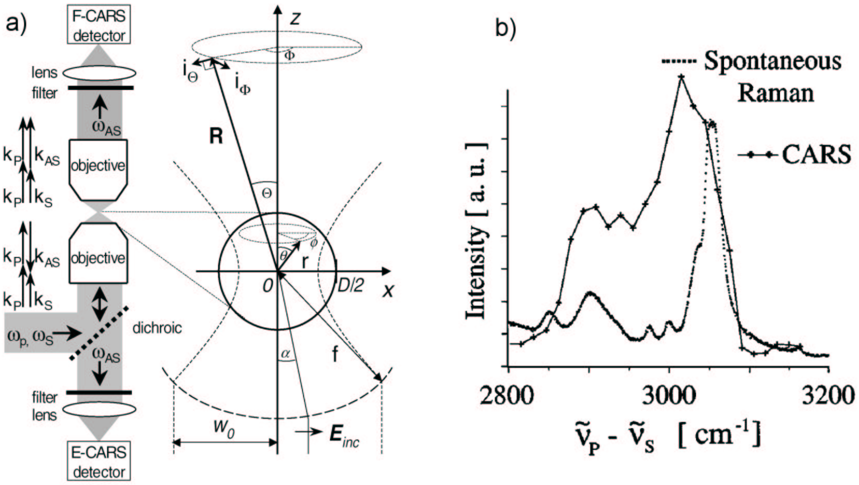
a)
F-CARS detector
lens
filter
ω_{AS}
k_P k_{AS}
objective
k_P k_S
k_P k_{AS}
objective
k_P k_S
ω_p, ω_S
dichroic
ω_{AS}
filter
lens
E-CARS detector
z
Φ
i_Θ
i_Φ
R
Θ
θ
φ
r
O
D/2
x
α
f
w_0
E_{inc}
b)
Spontaneous Raman
CARS
Intensity [a. u.]
2800
3000
3200
$\tilde{\nu}_P - \tilde{\nu}_S$ [cm^{-1}]

Fig. 6.9. (**a**) Optical Scheme of the collinear configurations for F– and E–CARS microscopy with collinear pump and Stokes beams and confocal detection in both forward and backward directions [73]. (**b**) CARS and spontaneous Raman spectra of a 910 nm polystyrene bead. For CARS, the pump wavelength (ν_P) was fixed at 854 nm and the Stokes wavelength (ν_S) was tuned from 1.12 to 1.17 µm. The spectral resolution is estimated to 60 cm^{-1} [77]

The 3–D imaging capability of CARS microscopy is shown in Fig. 6.10a where images of polystyrene beads are presented. The Raman transition probed is the CH ring stretch mode of polystyrene at 3038 cm^{-1}. The lateral spatial resolution obtained is around 300 nm.

If the sample is immersed in a liquid, the non–resonant background contribution from the solvent can significantly distort the CARS signal [78]. In such a case, since the overall thickness of the solution with the sample is much larger than the input wavelengths, the background contribution in F–CARS is much larger than in E–CARS. In fact, because of $|\Delta \boldsymbol{k}| \gg 2\pi/\lambda_{\mathrm{AS}}$, the background contribution in E–CARS from the solvent is largely suppressed. Figure 6.10b shows an E–CARS image taken at $\omega_{\mathrm{P}} - \omega_{\mathrm{S}}$=1570 cm^{-1} of a human living cell (75 × 75 μm^2 in size) in an aqueous solvent. It clearly exhibits many detailed features. The total imaging time was about 8 min.

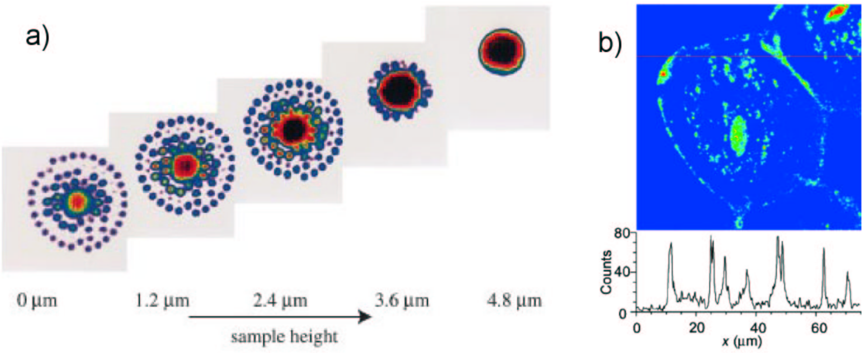

Fig. 6.10. (**a**) CARS section images (20 × 20 μm^2) of 910 nm polystyrene beads around a 4.3 μm bead taken at $\omega_{\mathrm{P}}-\omega_{\mathrm{S}}$=3038 cm^{-1}. Sectioning is in the z direction with 1.2 μm increments. The average powers of femtosecond pulses incident on the sample were 120 mW and 50 mW at 855 nm and 1.155 μm, respectively [77]. (**b**) E-CARS image with a Raman shift of 1570 cm^{-1} of an unstained human epithelial cell in an aqueous environment (size: 75 × 75 μm^2). The average powers of picosecond (f=100 kHz) Stokes (800 nm) and pump (741 nm) pulses were 1 an 2 mW, respectively. The lateral profile of the image displays features as small as 375 nm. Figure 6.10b is reprinted with permission from [10]. Copyright (2001) American Chemical Society

6.6 Multiphoton Excited Fluorescence Microscopy

Two–photon fluorescence microscopy was first developed by Webb and coworkers for applications to biological and medical sciences [9]. Its main asset comes from the 3–D imaging possibility to probe endogenous or exogenous fluorophores [79,80] with a good lateral and axial resolution using either the scanning or the confocal scheme. The technique has brought many new research opportunities to life science and is becoming a routine microscopy tool in many laboratories. Three–photon excited fluorescence microscopy has also been demonstrated. An excellent review on the subject can be found in [81].

Multiphoton–excited fluorescence microscopy offers several advantages over confocal one–photon fluorescence microscopy [82]. First, the pump beam is now in the transparent region that allows deeper probing into the sample [11,83]. The larger difference in wavelength between the pump and the fluorescence makes spectral filtering in signal detection much easier [84,85]. The much weaker absorption of pump radiation significantly reduces thermal distortion and photobleaching hazards on a sample. Second, because of the power dependence on the excitation intensity, the fluorescence originates mainly from the tight focal region. Therefore, sectioning of planes in 3–D imaging is limited only by the focal volume, and a confocal pinhole is often not required to suppress the out–of–focus fluorescence background. Probing volumes smaller than femto–liters have been reported .

Recent advances of multiphoton–excited fluorescence microscopy have been helped by the development of efficient fluorescent dyes with large multiphoton absorption cross–sections [86]. Work has been focused on improvement of the spatial resolution and reduction of the laser power needed. We review here a few most promising techniques and their combination with NSOM.

6.6.1 Two–Photon Excited Fluorescence (TPEF) Microscopy

We consider here both far–field and near–field versions of TPEF. Far–field TPEF is already widely used for characterization of biological samples because of its 3–D imaging capability. Near–field TPEF finds its interest in surface studies of microscope systems that allow simultaneous imaging of the surface topography and the different domains tagged by specific fluorophores.

Far–field TPEF Microscopy Two–photon–excited fluorescence yield from a sample is proportional to the number of molecules excited per unit time by two–photon absorption and the fluorescence efficiency η. It can be written as [79]

$$F(t) = \eta\sigma_2 \int\limits_V C(\boldsymbol{r}, t) I^2(\boldsymbol{r}, t) \mathrm{d}V, \tag{6.20}$$

where σ_2 is the two photon absorption cross–section, $C(\boldsymbol{r}, t)$ is the density of molecules in the ground state at $\boldsymbol{r}$ and t, and I is the exciting laser intensity. For common chromophores with excitation wavelength ranging from 690 nm to 1050 nm, σ_2 is about 10^{-48} to 10^{-50} cm^{4}s/photon [79]. Owing to the quadratic dependence of TPEF on laser intensity, the fluorescence in TPEF comes from a much reduced volume as compared to one–photon excited fluorescence [87]. Consider a tightly focused gaussian laser beam in a medium. If the beam attenuation in the medium is neglected, the input intensity distribution is given by

$$I(\rho, z) = \frac{2P}{\pi w_0^2(z)} \exp\left(\frac{-2\rho^2}{w_0^2(z)}\right), \tag{6.21}$$

where z is in the propagation direction with z=0 at the center of the focus and

$$w_0(z) = \frac{\lambda}{\pi(\mathrm{NA})} \sqrt{1 + \left(\frac{4\pi(\mathrm{NA})^2 z}{\lambda}\right)^2} \tag{6.22}$$

is the beam radius with λ being the wavelength and NA the numerical aperture. Taking the values NA=0.45 and λ=794 nm, the calculation shows that one–photon fluorescence comes equally from mainly from a 1.9 µm section in depth around the focal region [87]. TPEF microscopy images are often obtained with a scanning microscope. The laser beam is focused to a diffraction–limited beam waist of about 1 µm and is raster–scanned across a specimen. To improve the axial resolution, a confocal pinhole placed in front of the detector can be used as a spatial filter to selectively detect fluorescence from a particular section plane in the focal region. However, owing to the intrinsic sectioning capability of TPEF mentioned earlier, the pinhole is not always required [88]. Because of the small two–photon absorption cross section of fluorophores, focused excitation intensity in the MW cm^{-2} to GW cm^{-2} range is often needed for detectable fluorescence. For fast scanning, CW mode–locked (femtosecond pulsed) lasers with moderate peak power but low mean power are better suited.

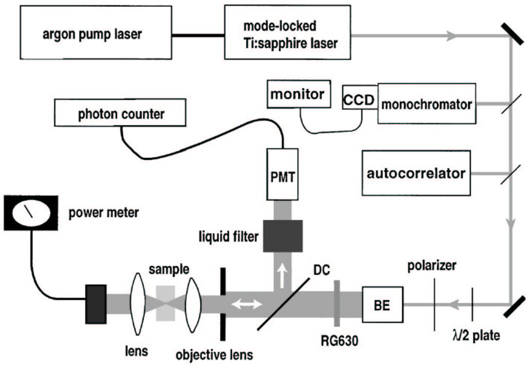

Fig. 6.11. Far–field TPEF microscopy setup. RG630, red–pass filter; BE, 5× beam expander; DC, dichroic mirror; PMT, photomultiplier tube [79]

Typical setup can be found in references [79,87,89]. An example is given in Fig. 6.11. Femtosecond pulses from a Ti:sapphire laser with an 80 MHz repetition rate is focused on a sample with a microscope objective of high NA. TPEF is epi–collected by the same objective and sent either directly to the detector [79,89] or after being spectrally resolved using a polychromator [87]. The 3–D image can be obtained by scanning of the laser focal spot on the sample in the $x - y$ plane with a galvanometer mirror and in the z direction by translation of the microscope objective [89] or the sample mounted on a piezoelectric ceramic. The spatial resolution of TPEF microscopy is similar to that of one–photon excited fluorescence microscopy despite the difference in excitation wavelengths, with typical values of 0.3 µm laterally and 0.9 µm axially [90]. The axial resolution can be improved by up to 50% with the addition of a confocal pinhole [91].

Near–Field TPEF Microscopy Coupling of NSOM microscopy with fluorescence measurement was initially developed for single–molecule spectroscopy imaging

[92] or time–resolved studies [93,94]. It has been used to probe single molecules, quantum dots and macromolecules on surfaces with a spatial resolution better than 20 nm [95–98].

Near–field TPEF microscopy has also been developed in recent years. Jenei *et al.* [99] used picosecond pulses from a Nd:YVO$_4$ laser to induce TPEF from labelling dye in a sample and an uncoated fiber tip for both excitation and collection of the fluorescent signal from the sample. Figure 6.12 shows their setup and the observed surface topography and TPEF image of a labelled mitochondria cell. The spatial resolution obtained was better than 200 nm. Similar resolution was achieved by Lewis *et al.* using femtosecond pulses from a Ti:sapphire laser to probe individual Rhodamine 6G molecules [100].

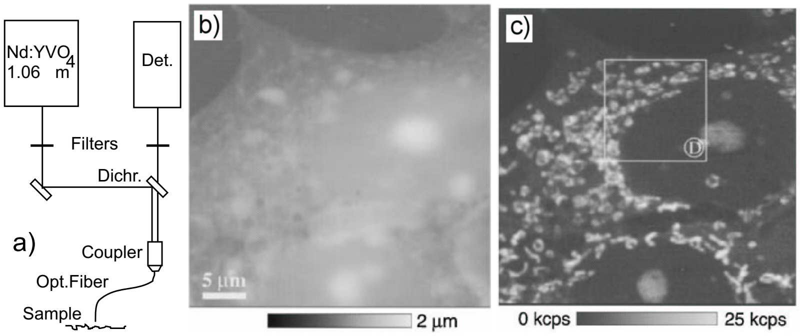

Fig. 6.12. (**a**) Optical configuration of TPEF combined with a scanning near–field optical microscope. The laser excitation of the sample is through an optical fiber tip which also collects the TPEF signal. The tip–sample distance is regulated by a shear force mechanism. (**b**) Topography of stained mitochondria cell. (**c**) TPEF image from the same area. Adapted from [99]

Hell *et al.*[15] and Kirsch *et al.*[101] showed that it is also possible to use a CW laser as the excitation source for TPEF microscopy and obtain good microscope images. An example is shown in Fig.6.13, where both far–field and near–field TPFE images of a chromosome stained with a dye are presented. The near–field image appears to have a better spatial resolution (150 nm).

Another variation of TPEF–NSOM has been developed by Sànchez *et al.* [102]. They used femtosecond laser pulses to illuminate a sample and a sharp gold tip near the surface to locally enhance the optical field at the sample (Fig. 6.14a). Such a local field enhancement can be very large and highly localized. In TPEF–NSOM, it strongly enhances the two–photon excitation and hence fluorescence from the sample area under the tip. (The same concept can be applied to other linear and nonlinear optical imaging techniques). Operating in both AFM and NSOM modes, the apparatus allows simultaneous imaging of surface topography and fluorescence microscopy. An example shown in Fig. 6.14b and c reveals features in fragments of photosynthetic membranes as well as J–aggregates with a resolution of 20 nm

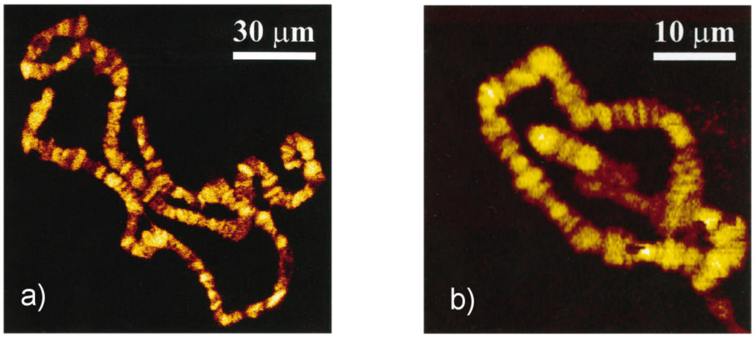
30 μm
a)
10 μm
b)

Fig. 6.13. (**a**) Far–field TPEF microscopy image of a stained chromosome using a CW ArKr laser excitation (λ=647 nm, P=100 mW, acquisition time 4 s). (**b**) Near–field TPEF microscopy image of the same stained chromosome [15]

that roughly corresponds to the tip apex. As pointed out by the authors, the use of a metal tip a few nanometer away from a fluorophore may quench the fluorescence. Therefore, proper fluorophores with rapid energy transfer should be used in such a technique. Kawata *et al.* have studied theoretically the optical field enhancement from metallic and dielectric tips of various shapes. Laser heating of the tips does not appear to be important. The lateral resolution of such an apertureless near–field microscope is estimated to be in the nanometer range [103].

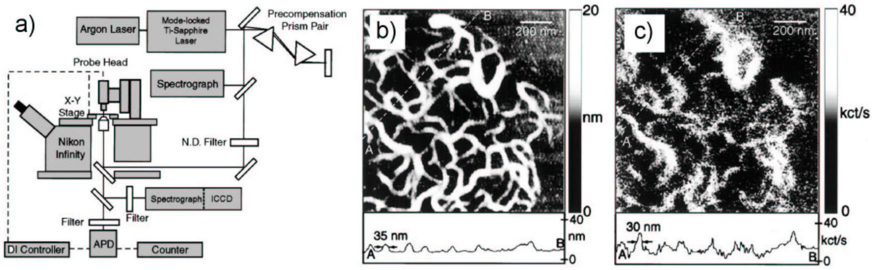
a)
Argon Laser
Mode-locked Ti-Sapphire Laser
Precompensation Prism Pair
Probe Head
Spectrograph
X-Y Stage
Nikon Infinity
N.D. Filter
Spectrograph
ICCD
Filter
Filter
DI Controller
APD
Counter
b)
B
200 nm
A
20
nm
0
35 nm
A
B
40
nm
0
c)
B
200 nm
A
40
kct/s
0
30 nm
A
B
40
kct/s
0

Fig. 6.14. (**a**) NSOM–TPEF set up with metallic tip excitation. The light source is a Ti:sapphire laser (λ=830 nm, τ=100 fs, f=76 MHz). The beam is sent into an inverted fluorescence microscope, reflected by a dichroic beam splitter and focused by a microscope objective (NA=1.4, 60 × 4) on the sample surface. The metal tip is centered onto the focal spot. The TPEF is collected by the same objective lens and detected either by an avalanche photodiode or analyzed by a spectrometer in conjunction with a CCD camera. Simultaneous topography image (**b**) and near–field TPEF image (**c**) of J–aggregates of pseudoisocyanine dye embedded in polyvinyl sulfate were obtained using the apparatus [102]

6.6.2 TPEF Far–Field Microscopy Using Multipoint Excitation

Introduced by Hell *et al.* [104,105] and Buist *et al.* [106], parallel microscopy imaging using a two–dimensional microlens array has been proved to be a powerful instrument for fast image acquisition without increasing excitation intensity. This is possible because TPEF is confined to the small focal volumes. The microlens array splits an incident laser beam into beamlets that separately focus into the sample; the number of focal points equals to the number of microlenses. Fluorescent signals from the focal regions are collected by a 2–D photodetection system. Shown in Fig. 6.15 is the apparatus developed by Bewersdorf *et al.* that permits real–time 3–D imaging with high efficiency and resolution [105]. The expanded beam from a femtosecond laser illuminates a section of microlenses etched on a disk each having a diameter of 460 µm and a focal length of 6 mm. The overall arrangement of the microlenses on the disk form a pattern of spirals with 10 rows. The multiple beamlets pass through intermediate optics and form an array of independent foci on the sample with the help of an objective lens that is also used for collection and mapping of fluorescence from the multiple foci onto a CCD camera. Rotation of the microlens disk allows for scanning of foci in a sample plane. The image acquisition speed depends on the number of lenses arranged in rows and the rotation frequency of the disk. Bewersdorf *et al.* have used an acquisition speed 40 to 100 times faster than that of a single–beam scanning TPEF, permitting real–time TPEF imaging of living cells. The spatial resolution they obtained was similar to those of conventional TPEF microscope with an axial resolution of about 0.84 µm when an oil immersion objective lens was used.

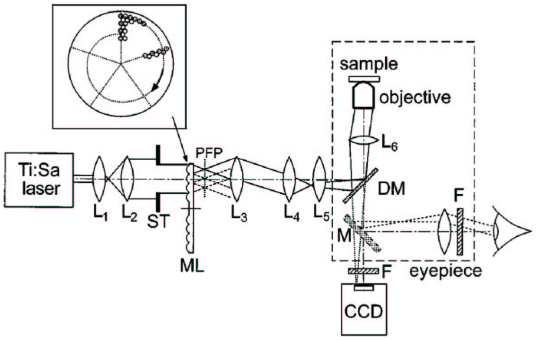

Fig. 6.15. Optical setup of a multifocal multipoint microscope for real–time direct–view TPEF microscopy. L: lenses, ML: microlens disk, M: mirror, DM: dichroic mirror. The inset shows the array of a spiral arrangement of microlenses on the disk [105]

6.6.3 4–Pi Confocal TPEF Microscopy

4–Pi confocal microscopy is 3–D TPEF microscopy technique developed to improve the axial resolution of far–field microscopy [107]. An axial resolution of about 100 nm has been demonstrated [108]. The scheme involves excitation of the sample by counter–propagating beams through two objective lenses with high numerical aperture (Fig. 6.16a). The overall excitation aperture of the system would approach 4π if the aperture extended by each lens were 2π. The acronym of the system 4–Pi was chosen as a reminder of this arrangement.

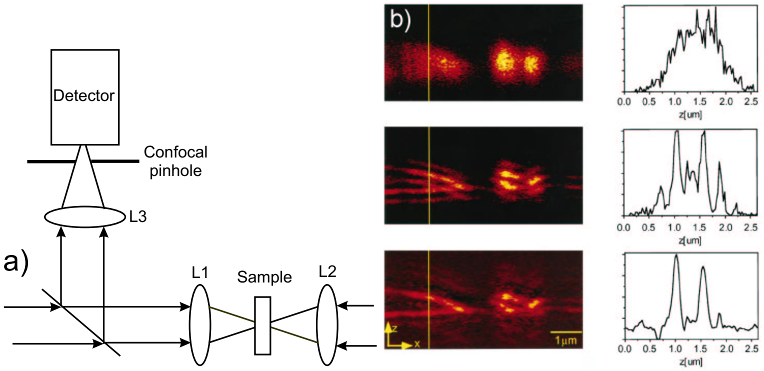

Fig. 6.16. (**a**) Setup of the TPEF 4–Pi confocal microscope. The numerical aperture of the 100× oil immersion objectives is 1.4 [109]. (**b**) Microscopy images obtained with various schemes: two photon confocal (top), two photon 4–Pi confocal (center), two photon 4–Pi confocal after side–lobe removal (bottom). The right column shows the intensity profiles of the fluorescence along the lines indicated in the respective images [108]

The two counter–propagating beams interfering in the focal region should yield an intensity distribution with a main peak several times narrower in the axial direction than that obtainable by a single focused beam. Furthermore, fluorescence from secondary interference peaks (axial lobes) along the axis in the focal region can be significantly reduced by a confocal pinhole (Fig. 6.16a) and by a deconvolution procedure using a restoration algorithm [109]. Figure 6.16b shows as example axial images of a fibroblast cell using various schemes (confocal, 4–Pi confocal, 4–Pi confocal with axial lobes removed). The excitation source was a mode–locked femtosecond Ti:sapphire. The 4–Pi confocal microscopy image with axial lobes suppressed obviously has the best axial resolution. It reveals details on a scale less than 200 nm.

6.6.4 Simultaneous SHG/TPEF Microscopy

SHG and TPEF can be simultaneously generated from a sample by a focused beam and detected in the same microscopy system. Both processes have an output proportional to the square of the input laser intensity, but one is coherent and the other incoherent. If they are pumped by the same laser input, then, as shown in Fig. 6.17a, both experience the same two–photon resonant excitation. However, SHG is surface–specific in media with inversion symmetry and TPEF is not. Thus the two processes can provide complementary information about the sample. Lewis and coworkers [37,38] and Moreaux *et al.* [36,89,110], have used combined SHG/TPEF microscopy to study biological membranes. In the setup of Moreaux *et al.*, femtosecond pulses from a Ti:sapphire were used for excitation of a sample through a microscope objective. The SHG output in the forward direction was collected by a lens while TPEF was epi–collected with the help of a dichroic mirror. Three dimensional SHG and TPEF images were obtained by scanning the laser focal spot in the $x - y$ plane with galvanometer mirrors and in the axial direction by translation of the objective. Presented in Figs.6.17(b) and (c) are vesicles images acquired in 1.5 s with an excitation power less than 1 mW [89]. They provide an excellent example of complementarity of SHG and TPEF: the adhesion between the two vesicles appears to be centrosymmetric as it contributes to TPEF but not to SHG.

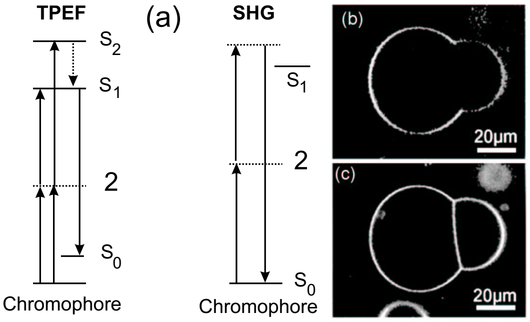

Fig. 6.17. (**a**) Level diagrams describing two–photon excited fluorescence and second harmonic generation. (**b**) SHG and (**c**) TPFE images of labelled vesicles excited by laser input at λ= 880 nm (τ=80 fs, f=80 MHz, $P \leq 1$ mW) [89]

6.6.5 Three–Photon–Excited Fluorescence Microscopy

Three–photon–excited fluorescence microscopy has also been demonstrated. The cubic dependence of fluorescence on the local input laser intensity allows further improvement of the spatial resolution as compared to TPEF. For samples such as amino acids, proteins and neurotransmitters that are susceptible to photodamage by one–photon absorption in the ultra–violet and residual absorption in the visible–red range, the three–photon–excited fluorescence scheme with a near–infrared input beam could avoid the damage and seems to be most suitable for microscopy. Using femtosecond Ti:sapphire laser pulses for excitation, Gryczynski *et al.* successfully imaged the triptophan residues [111] and Maiti *et al.* imaged neurotransmitters in living cells [85].

A lateral and axial resolution of ~ 0.2 and ~ 0.6 µm has been achieved [80]. The main disadvantage of the technique is the narrow window of operation. Because the three–photon absorption cross–section of a sample is generally very small (10^{-75}–10^{-84} cm^6 s^2 photon^{-2}), high peak laser intensity is required for excitation that likely causes damage of the sample.

6.6.6 Stimulated–Emission–Depletion (STED) Fluorescence Microscopy

Recently, Klar *et al.* proposed and demonstrated an interesting idea that can significantly improve the spatial resolution of fluorescence microscopy [112]. It involves fluorescence quenching of excited molecules at the rim of the focal spot through stimulated emission thus significantly reducing the focal volume that emits fluorescence. This is accomplished by passing the quenching laser beam through an optical phase plate, yielding a focused wave front that produces by destructive interference a central minimum at the focal point. In the experiment (Fig. 6.18a), two synchronized pulses from a Ti:sapphire laser/optical parametric oscillator system with a 76 Mhz repetition rate were used: a visible pulse with a 0.2 ps pulsewidth for excitation followed by a near–infrared pulse with a 40 ps pulsewidth for fluorescence quenching. The visible pulse at λ=560 nm originated from the optical parametric oscillator with an intracavity frequency doubler and the near–infrared pulse at λ=765 nm came directly from the laser. The fluorescence was epi–collected by an avalanche photodiode after passing through a confocal pinhole. The lateral and axial resolutions obtained were ~100 nm, which is an improvement of a factor 5 in the axial direction and 2 in the lateral one, compared to ordinary confocal microscope (Fig. 6.18(b) and (c)).

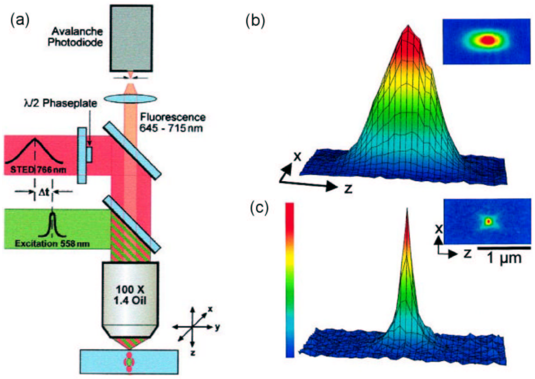

Fig. 6.18. (**a**) STED microscope setup. Excitation pulse is followed by fluorescence quenching pulse. Fluorescence is then detected after passing through dichroic filters and a confocal pinhole. (**b**) and (**c**), Intensity distributions of fluorescence along x and z (axial direction) in confocal and in confocal STED microscopy, respectively. The latter has an axial width of 97 nm which is 5 times narrower than in (**b**) [112] (Copyright (2000) National Academy of Sciences, U.S.A.)

Besides the improvement on spatial resolution which compete with most near–field optical microscopes, STED microscopy can also find other important applications in studies of ultrafast dynamics. The ultrafast control of fluorescence under microscopy conditions opens new opportunities for transient microscopy and spectroscopy of nano–objects. It should also have interesting perspectives in single molecule spectroscopy such as control of individual excited molecules with femtosecond time resolution [113].

6.7 Conclusion

In this contribution, we have briefly surveyed the field of nonlinear optical microscopy and presented a few examples of contemporary applications. The survey is by no means complete. The field is still at its infant stage. Further development of the techniques and their applications can be anticipated. As in the past, future advances would benefit from having better lasers, better optics and optical systems and better photodetectors. For example, an efficient high–speed detection and data acquisition system incorporated with an optimized pulse laser excitation scheme would allow *in–situ* probing of time–dependent surface reactions on nanostructures or *in–vivo* study of biological cells. Compared to linear–optics, nonlinear optics has the advantage that it probes a larger domain of material properties. SHG and SFG, for example, are unique in their abilities to probe selectively surfaces and interfaces. However, nonlinear optics also has the disadvantages that it generally requires stronger input laser intensity and the effects are more complex. The latter point is important for interpretation of the observed microscopy images. In particular, a clear understanding of the effects in near–field microscopy is essential for the future progress of nonlinear NSOM.

Acknowledgments
Work was supported by the Director, Office of Energy Research, Office of Basic Energy Sciences, Materials Science Division, of the US Departement of Energy under contract No.DE–AC03–765F00098. F.L.L. gratefully acknowledges the Centre National de la Recherche Scientifique (C.N.R.S., France) for his support during his stay at the University of California at Berkeley.

References

1. P.T.C. So: Opt. Express **3**, 312 (1998)
2. X. Zhuang, P.B. Miranda, D. Kim, Y.R. Shen: Phys. Rev. B **59**, 12632 (1999)
3. X. Wei, S.–C. Hong, X. Zhuang, T. Goto, Y.R. Shen: Phys. Rev. E **62**, 5160 (2000)
4. V. Vogel, Y.R. Shen: Annu. Rev. Mater. Sci. **21**, 515 (1991)
5. M. Flörsheimer: Phys. Status Solidi (a) **173**, 15 (1999)
6. G.J. Simpson: Appl. Spectrosc. **55**, 16 (2001)
7. J.A. Squier, M. Müller, G.J. Brakenhoff, K.R. Wilson: Opt. Express **3**, 315 (1998)
8. E.O. Potma, W.D. de Boej, D.A. Wiersma: J. Opt. Soc. Am. B **17**, 1678 (2000)
9. W. Denk, J.H. Strickler, W.W. Webb: Science **248**, 73 (1990)
10. J.–X. Cheng, A. Volkmer, L.D. Book, X.S. Xie: J. Phys. Chem. B **105**, 1277 (2001)
11. K. König: J. Microsc. – Oxford **200**, 83 (2000)
12. S.I. Bozhevolnyi, T. Geisler: J. Opt. Soc. Am. A **15**, 2156 (1998)
13. Y. Shen, J. Swiatkiewicz, J. Winiarz, P. Markowicz, P.N. Prasad: Appl. Phys. Lett. **77**, 2946 (2000)

14. R.D. Schaller, J.C. Johnson, R.J. Saykally: Anal. Chem. **72**, 5361 (2000)
15. S.W. Hell, M. Booth, S. Wilms, C.M. Schnetter, A.K. Kirsch, D.J. Arndt–Jovin, T.M. Jovin: Opt. Lett. **23**, 1238 (1998)
16. Y.R. Shen: *The Principles of Nonlinear Optics* (Wiley, New York 1984)
17. R. Boyd: *Nonlinear Optics* (Academic, New York 1992)
18. M. Oh–e, S.C. Hong, Y.R. Shen: J. Phys. Chem. B **104**, 7455 (2000)
19. S.–C. Hong, M. Oh–e, X. Zhuang, Y.R. Shen, J.J. Ge, F.W. Harris, S.Z.D. Cheng: Phys. Rev. E **63**, 517061 (2001)
20. R. Hellwarth, P. Christensen: Appl. Optics **14**, 247 (1975)
21. G.T. Boyd, Y.R. Shen, T.W. Hänsch: Opt. Lett. **11**, 97 (1986)
22. K.A. Schultz, E.G. Seebauer: J. Chem. Phys. **97**, 6958 (1992)
23. K.A. Schultz, I.I. Suni, E.G. Seebauer: J. Opt. Soc. Am. B **10**, 546 (1993)
24. M.S. Johal, A.N. Parikh, Y. Lee, J.L. Casson, L. Foster, B.I. Swanson, D.W. McBranch, D.Q. Li, J.M. Robinson: Langmuir **15**, 1275 (1999)
25. N. Kato, K. Saito, Y. Uesu: Thin solid films **335**, 5 (1999)
26. S.B. Bakiamoh, G.J. Blanchard: Langmuir **17**, 3438 (2001)
27. L. Smilowitz, Q.X. Jia, X. Yang, D.Q. Li, D. McBranch, S.J. Buelow, J.M. Robinson: J. Appl. Phys. **81**, 2051 (1997)
28. Y. Sonoda, G. Mizutani, H. Sano, S. Ushioda, T. Sekiya, S. Kurita: Jap. J. Appl. Phys. **39**, L253 (2000)
29. H. Sano, T. Shimizu, G. Mizutani, S. Ushioda: J. Appl. Phys. **87**, 1614 (2000)
30. K. Pedersen, S.I. Bozhevolnyi, J. Arentoft, M. Kristensen, C. Laurent–Lund: J. Appl. Phys. **88**, 3872 (2000)
31. I.I. Suni, E.G. Seebauer: J. Chem. Phys. **100**, 6772 (1994)
32. S. Kurimura, Y. Uesu: J. Appl. Phys. **81**, 369 (1996)
33. F. Rojo, F. Agulló–lópez, B. del Rey, T. Torres: J. Appl. Phys. **84**, 6507 (1998)
34. S.E. Kapphan: J. Lumin. **83**, 411 (1999)
35. I. Freund, M. Deutsch: Opt. Lett. **11**, 94 (1986)
36. L. Moreaux, O. Sandre, S. Charpak, M. Blanchard–Desce, J. Mertz: Biophys. J. **80**, 1568 (2001)
37. P.J. Campagnola, M.–D. Wei, A. Lewis, L.M. Loew: Biophys. J. **77**, 3341 (1999)
38. C. Peleg, A. Lewis, M. Linial, M. Loew: P. Natl. Acad. Sci. USA **96**, 6700 (1999)
39. M. Flörsheimer, D.H. Jundt, H. Looser, K. Sutter, M. Küpfer, P. Günter: Ber. Bunsenges. Phys. Chem. **9**, 521 (1994)
40. M. Flörsheimer, M. Bösch, Ch. Brillert, M. Wierschem, H. Fuchs: J. Vac. Sci. Technol. B **15**, 1564 (1997)
41. M. Flörsheimer, M. Bösch, Ch. Brillert, M. Wierschem, H. Fuchs: Supramol. Sci. **4**, 255 (1997)
42. M. Flörsheimer, C. Brillert, H. Fuchs: Langmuir **15**, 5437 (1999)
43. Y. Guo, P.P. Ho, H. Savage, D. Harris, P. Sacks, S. Schantz, F. Liu, N. Zhadin, R.R. Alfano: Opt. Lett. **22**, 1323 (1997)
44. R. Gauderon, P.B. Lukins, C.J.R. Sheppard: Opt. Lett. **23**, 1209 (1998)
45. M. Cernusca, M. Hofer, G.A. Reider: J. Opt. Soc. Am. B **15**, 2476 (1998)
46. G. Berkovic, Y.R. Shen, G. Marowsky, R. Steinhoff: J. Opt. Soc. Am. B **6**, 205 (1989)
47. G.A. Reider, M. Cernusca, M. Hofer: Appl. Phys. B. – Lasers O. **68**, 343 (1999)
48. P. Rechsteiner, J. Hulliger, M. Flörsheimer: Chem. Mater. **12**, 3296 (2000)
49. I.I. Smolyaninov, A.V. Zayats, C.C. Davis: Phys. Rev. B **56**, , (9)2901997
50. I.I. Smolyaninov, A.V. Zayats, C.C. Davis: Opt. Lett. **22**, , (1)5921997
51. I.I. Smolyaninov, C.H. Lee, C.C. Davis: J. Microsc. – Oxford **194**, , (4)26 1999

52. S.I. Bozhevolnyi, B. Vohnsen, K. Pedersen: Opt. Commun. **150**, 49 (1998)
53. K. Karrai, R.D. Grobber: Appl. Phys. Lett. **66**, 1842 (1995)
54. B. Vohnsen, S.I. Bozhevolnyi: J. Microsc. – Oxford **202**, 244 (2001)
55. A. Liu, G.W. Bryant: Phys. Rev. B **59**, 2245 (1999)
56. S.I. Bozhevolnyi, V.Z. Lozovski: Phys. Rev. B **16**, 11139 (2000)
57. S.I. Bozhevolnyi, V.Z. Lozovski, K. Pedersen, J.M. Hvam: Phys. Status Solidi(a) **175**, 331 (1999)
58. A.V. Zayats, T. Kalkbrenner, V. Sandoghdar, J. Mlynek: Phys. Rev. B **61**, 4545 (2000)
59. Z.–Y. Li, B.–Y. Gu, G.Z. Yang: Phys. Rev. B **59**, 12622 (1999)
60. P.B. Miranda, Y.R. Shen: J. Phys. Chem. B **103**, 3292 (1999)
61. X. Wei, P.B. Miranda, Y.R. Shen: Phys. Rev. Lett. **86**, 1554 (2001)
62. R.D. Schaller, R.J. Saykally: Langmuir **17**, 2055 (2001)
63. B. Humbert, J. Grausem, A. Burneau, M. Spajer, A. Tadjeddine: Appl. Phys. Lett. **78**, 135 (2001)
64. Y. Barad, H. Eisenberg, M. Horowitz, Y. Silberberg: Appl. Phys. Lett. **70**, 922 (1997)
65. T.Y.F. Tsang: Phys. Rev. A **52**, 4116 (1995)
66. D. Yelin, Y. Silberberg, Y. Barad, J.S. Patel: Appl. Phys. Lett. **74**, 3107 (1999)
67. C.–K. Sun, S.–W. Chu, S.–P. Tai, S. Keller, U.K. Mishra, S.P. DenBaars: Appl. Phys. Lett. **77**, 2331 (2000)
68. M. Müller, J. Squier, C.A. De Lange, G.J. Brakenhoff: J. Microsc. – Oxford **197**, 150 (2000)
69. M. Müller, J. Squier, K.R. Wilson, G.J. Brakenhoff: J. Microsc. – Oxford **191**, 266 (1998)
70. L. Canioni, S. Rivet, L. Sarger, P. Barille, P. Vacher, P. Voisin: Opt. Lett. **26**, 515 (2001)
71. J.A. Squier, M. Müller: Appl. Optics **38**, 5789 (1999)
72. G.L. Eesley: *Coherent Raman Spectroscopy* (Pergamon, New York 1981)
73. A. Volkmer, J.–X. Cheng, X.S. Xie: Phys. Rev. Lett. **87**, 23901 (2001)
74. M.D. Duncan, J. Reintjes, T.J. Manuccia: Opt. Lett. **7**, 350 (1982)
75. M.D. Duncan, J. Reintjes, T.J. Manuccia: Opt. Commun. **50**, 307 (1984)
76. M.D. Duncan, J. Reintjes, T.J. Manuccia: Opt. Express **24**, 352 (1985)
77. A. Zumbusch, G.R. Holtom, X.S. Xie: Phys. Rev. Lett. **82**, 4142 (1999)
78. M. Hashimoto, T. Araki, S. Kawata: Opt. Lett. **25**, 1768 (2000)
79. C. Xu, W.W. Webb: J. Opt. Soc. Am. B **13**, 481 (1996)
80. C. Xu, W. Zipfel, J.B. Shear, R.M. Williams, W.W. Webb: P. Natl. Acad. Sci. USA **93**, 10763 (1996)
81. J.R. Lakowicz: *Topics in Fluorescence Spectroscopy: Nonlinear and Two–Photon Induced Fluorescence* (Plenum, New York 1997)
82. D.W. Piston, D.R. Sandison, W.W. Webb: SPIE **1640**, 379 (1992)
83. J. Ying, F. Liu, R.R. Alfano: Appl. Optics **39**, 509 (2000)
84. J.R. Lakowicz and I. Gryczynski, H. Malak, P. Schrader, P. Engelhardt, H. Kano, S.W. Hell: Biophys. J. **72**, 567 (1997)
85. S. Maiti, J.B. Shear, R.M. Williams, W.R. Zipfel, W.W. Webb: Science **275**, 530 (1997)
86. M.Barzoukas, M. Blanchard–Desce: J. Chem. Phys. **113**, 3951 (2000)
87. S. Andersson–Engels, I. Rokahr, J. Carlsson: J. Microsc. – Oxford **176**, 195 (1994)
88. R. Gauderon, P.B. Lukins, C.J.R. Sheppard: Microsc. Res. Techniq. **47**, 210 (1999)
89. L. Moreaux, O. Sandre, M. Blanchard–Desce, J. Mertz: Opt. Lett. **25**, 320 (2000)
90. W. Denk, D.W. Piston, W.W. Webb: ‘Two–photon molecular excitation in laser–scanning microscopy’, In: *Handbook of Biological Confocal Microscopy*, ed. by J.B. Pawley (Plenum, New York 1995) pp. 445–458

91. E. Stelzer, S. Hell, S. Lindek, R. Stricker, R. Pick, C. Storz, G. Ritter, N. Salmon: Opt. Commun. **104**, 223 (1994)
92. E. Betzig, R.J. Chichester: Science **262**, 1422 (1993)
93. X.S. Xie, R.C. Dunn: Science **265**, 361 (1994)
94. G. Parent, D. Van Labeke, F.I. Baida: J. Microsc. – Oxford **202**, 296 (2001)
95. R. Zenobi, V. Deckert: Angew. Chem. Int. Ed. **39**, 1746 (2000)
96. P.K. Yang, J.Y. Huang: Opt. Commun. **173**, 315 (2000)
97. H. Muramatsu, K. Homma, N. Yamamoto, J. Wang, K. Sakata–Sogawa, N. Shimamoto: Materials Science and Engineering C **12**, 29 (2000)
98. N. Hosaka, T. Saiki: J. Microsc. – Oxford **202**, 362 (2001)
99. A. Jenei, A.K. Kirsch, V. Subramaniam, D.J. Arndt–Jovin, T.J. Jovin: Biophys. J. **76**, 1092 (1999)
100. M.K. Lewis, P. Wolanin, A. Gafni, D.G. Steel: Opt. Lett. **23**, 1111 (1998)
101. A.K. Kirsch, V. Subramaniam, G. Striker, C. Schnetter, D.J. Arndt–Jovin, T.M. Jovin: Biophys. J. **75**, 1513 (1998)
102. E.J. Sánchez, L. Novotny, X.S. Xie: Phys. Rev. Lett. **82**, 4014 (1999)
103. Y. Kawata, C. Xu, W. Denk: J. Appl. Phys. **85**, 1294 (1999)
104. S.W. Hell, V. Andresen: J. Microsc. – Oxford **202**, 457 (2001)
105. J. Bewersdorf, R. Pick, S.W. Hell: Opt. Lett. **23**, 655 (1998)
106. A.H. Buist, M. Müller, J. Squier, G.J. Brakenhoff: J. Microsc. – Oxford **192**, 217 (1998)
107. P.E. Hänninen, S.W. Hell, J. Salo, E. Soini: J. Appl. Phys. **66**, 1698 (1995)
108. M. Schrader, K. Bahlmann, G. Giese, S.W. Hell: Biophys. J. **75**, 1659 (1998)
109. M. Schrader, S.W. Hell, H.T.M. van der Voort: J. Appl. Phys. **84**, 4033 (1998)
110. L. Moreaux, O. Sandre, J.W. Mertz: J. Opt. Soc. Am. B **17**, 1685 (2000)
111. I. Gryczynski, H. Malak, J.R. Lakowicz: Biospectroscopy **2**, 9 (1996)
112. T.A. Klar, S. Jakobs, M. Dyba, A. Egner, S.W. Hell: P. Natl. Acad. Sci. USA **97**, 8206 (2000)
113. M. Dyba, T.A. Klar, S. Jakobs, S.W. Hell: Appl. Phys. Lett. **77**, 597 (2000)